JOURNAL OF THERMOPHYSICS AND HEAT TRANSFER
Vol. 10, No. 2, April–June 1996

Two- and Three-Dimensional Analysis of Hypersonic Nonequilibrium Low-Density Flows

Roop N. Gupta*
NASA Langley Research Center, Hampton, Virginia 23681-0001

Flowfield results have been obtained for hypersonic, low-density, two- and three-dimensional, nonequilibrium viscous shock-layer flows. Three-dimensional calculations are performed for sphere–cone-shaped bodies at various angles of attack. Recently obtained surface and shock-slip boundary conditions are implemented to account for the low-density effects. These boundary conditions may also be employed with the Navier–Stokes equations with or without a shock-fitting solution technique. A method is suggested for obtaining the input shock shape for the three-dimensional nonequilibrium viscous flow. This approach gives superior convergence of results, especially under low-density flow conditions, and makes the VSL method self-starting. The analytic algebraic grid implemented with the equations does not add any numerical dissipation. Obtained results show the effect of low density on the surrounding flowfield and surface quantities for a hypervelocity vehicle. Good agreement is obtained with the available numerical results (including the direct simulation Monte Carlo predictions) and experimental data for the low-density flight conditions.

Nomenclature

C_i = mass fraction of species i, ρ_i^*/ρ^*
C_H = heat transfer coefficient, $2q_w^*/\rho_\infty^* U_\infty^{*3}$
C_p = frozen specific heat of mixture, $\Sigma_i\, C_i C_{p,i}$
$C_{p,i}$ = specific heat of species i, $C_{p,i}^*/C_{p,\infty}^*$
D_{ij}^* = binary diffusion coefficient
$\hat{e}_x, \hat{e}_r, \hat{e}_\phi$ = unit vectors along x, r, ϕ
h = mixture enthalpy, $\Sigma_i\, C_i h_i$
h_i = enthalpy of species i, h_i^*/U_∞^{*2}
h_1, h_2, h_3 = scale factors for a surface-normal coordinate system
K = thermal conductivity of mixture, $K^*/\mu_{\text{ref}}^* C_{p,\infty}^*$
Le_i = Lewis number, $\rho^* D_{ij}^* C_p^*/K^*$
M_∞ = freestream Mach number
$\hat{N}$ = vector normal to the shock surface, Figs. 2a and 2b
NS = number of reacting species
n_{sh} = shock standoff distance, n_{sh}^*/R_N^*
Pr = Prandtl number, $\mu^* C_p^*/K^*$
p = pressure, $p^*/\rho_\infty^* U_\infty^{*2}$
Re_∞ = Reynolds number, $\rho_\infty^* U_\infty^* R_N^*/\mu_\infty^*$
R_N^* = nose radius
s, n, ϕ = nondimensional surface-oriented coordinate system, Fig. 1, $s = s^*/R_N^*$, $n = n^*/R_N^*$, $\phi = \phi$, deg
T = temperature, T^*/T_{ref}^*
$\hat{T}$ = vector tangent to the bow shock, Figs. 2a and 2b
T_{ref}^* = reference temperature, $U_\infty^{*2}/C_{p,\infty}^*$
U_∞^* = freestream velocity
u, v, w = streamwise, normal, and crossflow velocity components nondimensionalized by the freestream velocity
W_i = molecular weight of species i
$\bar{W}$ = molecular weight of mixture
$\dot{w}_i$ = mass rate of formation of species i, $\dot{w}_i^* R_N^*/\rho_\infty^* U_\infty^*$
x^* = axial distance from blunt nose, body axis
α = angle of attack
β = shock angle in meridional plane, Fig. 1
β_{sh} = angle between the component of freestream velocity and the total velocity behind the shock in meridional plane, Fig. 2c
γ_i = recombination coefficient for species i
$\bar{\gamma}$ = ratio of specific heats, C_p^*/C_v^*
Δh_i^{*f} = heat of formation of species i
$\Delta\xi, \Delta\phi$ = step sizes in the streamwise and crossflow directions
ε = Reynolds number parameter, $\varepsilon^2 = \mu_{\text{ref}}^*/\rho_\infty^* U_\infty^* R_N^*$
$\bar{\eta}$ = normalized surface-normal coordinate, n/n_{sh}
θ = accommodation coefficient
θ_2' = angle by which the streamline is turned in crossing the shock, Fig. 2b
θ_ξ = body angle in the streamwise direction
κ_ξ, κ_ζ = body curvature in streamwise and crossflow direction, $\kappa_\xi = \kappa_\xi^* R_N^*$, $\kappa_\zeta = \kappa_\zeta^* R_N^*$
μ_{ref}^* = reference viscosity, $\mu^*(T_{\text{ref}}^*)$
ξ, η, ζ = transformed surface-oriented coordinate, $\xi \equiv s$, $\eta = g(\bar{\eta})$, $\zeta \equiv \phi$
ρ = density, ρ^*/ρ_∞^*
σ' = angle between the freestream velocity vector and $\hat{T}$, Fig. 2b
ϕ = crossflow plane or azimuthal angle measured from windward plane

Subscripts
body = coordinate system with origin at the geometric stagnation point
i = ith species
s = Knudsen-layer edge value
sh = shock value
TP = tangency point
w = wall value
wind = coordinate system with origin at the aerodynamic stagnation point
∞ = freestream condition

Received Sept. 8, 1995; revision received Nov. 27, 1995; accepted for publication Dec. 1, 1995.

*Senior Research Engineer, Aerothermodynamics Branch, Gas Dynamics Division. Associate Fellow AIAA.

Superscripts

s = Knudsen-layer edge value
$'$ = derivative with respect to ξ
$*$ = dimensional quantity
$-$ = normalized variable
$\sim$ = shock-oriented quantities
$\hat{}$ = vector quantity

Introduction

SINCE most of the currently planned and future hypersonic vehicles will be operating in the upper atmosphere, it is important to quantify the low-density effects. This work is intended to analyze these effects for axisymmetric bodies at angle of attack with finite rate chemistry.

Among the computational methods available for predicting hypersonic finite rate blunt body flows, the viscous shock-layer (VSL) technique is a very effective and efficient tool[1,2] for attached flows. Even at large angles of attack, flow in the nose region of a vehicle stays generally attached in the crossflow plane. Therefore, the VSL methods can be employed to provide the starting solution for an accurate afterbody solution scheme (such as a parabolized Navier–Stokes scheme[2]). Further, the nonequilibrium VSL technique[3] can provide the blunt-body (nose-regions) solutions at a small fraction of the computational time and storage needed for a nonequilibrium Navier–Stokes scheme.[4]

Swaminathan et al.[5] and Song et al.[6] have considered the low-density effects through surface- and shock-slip formulations in their analyses of the three-dimensional viscous shock-layer flows. Their shock-slip formulation, however, did not account for derivatives of the shock quantities in the shock-oriented coordinate system, among other errors. This introduces errors in analyzing flows beyond the stagnation line. They also retained the errors (such as inconsistent gas-surface interaction model and incorrect evaluation of the diffusion flux) of Ref. 7 in the specification of surface slip boundary conditions as explained in Ref. 8 (p. 9). Further, the frozen-flow approximation employed in the shock-slip boundary conditions of Refs. 5 and 6 is not a very physically appealing approximation for a thick shock under the low-density conditions, where the characteristic flow times are large enough to initiate chemical activity through the shock. Unlike Refs. 5 and 6, it is also desirable to solve the flowfield equations with equal step size in the computational plane to keep the same order of accuracy for the computed results. Finally, to make the computer code robust and to speed up global convergence, the input shock shape for the low-density nonequilibrium viscous shock-layer calculations should be obtained from a corresponding approximate flowfield calculation in place of using an equilibrium shock shape.[5,6]

This study was carried out by employing a three-dimensional viscous shock-layer code[9] with the recently obtained surface- and shock-slip boundary conditions. Flow governing equations in the code, however, are recast in terms of an analytical grid, which has a zero numerical dissipation of its own. The latest transport properties are employed for the air species with appropriate mixing laws for the ionized mixture. Comparisons are made with other numerical predictions [including the direct simulation Monte Carlo (DSMC) results] and the available flight data.

Analysis

The VSL equations are obtained from the steady-state Navier–Stokes equations by keeping terms up to second order in the inverse square root of the Reynolds number ε. Consequently, one set of equations is solved for both the inviscid and viscous regions. Further, parabolic approximations are made in the streamwise and crossflow directions. Thus, the equations can be solved in both directions using marching techniques that are efficient in terms of computer time and storage requirements. The equations are limited, however, to attached flows in both directions. A three-dimensional VSL code, originally developed in Ref. 9, serves as the basis for this study.

Governing Equations

The viscous shock-layer equations for a reacting multicomponent gas mixture are obtained from the basic conservation equations[10,11] by the method mentioned earlier. These equations in the orthogonal, body-oriented transformed coordinates (Fig. 1) and normalized form are provided here. Most of the flowfield variables are normalized with their local shock values to keep them of the order of 1. The normal coordinate is normalized with the local shock standoff distance to obtain a constant number of grid points between the body and shock. The second-order partial differential equations (PDEs), namely, ξ (or s) momentum, ζ (or ϕ) momentum, energy, and the species continuity equations are written in the following form:

$$\frac{\partial^2 W}{\partial \eta^2} + \frac{\left(A_0 \dfrac{\partial^2 g}{\partial \bar{\eta}^2} + A_1 \dfrac{\partial g}{\partial \bar{\eta}}\right)}{A_0 \left(\dfrac{\partial g}{\partial \bar{\eta}}\right)^2} \frac{\partial W}{\partial \eta} + \frac{A_2 W}{A_0 \left(\dfrac{\partial g}{\partial \bar{\eta}}\right)^2} + \frac{A_3}{A_0 \left(\dfrac{\partial g}{\partial \bar{\eta}}\right)^2} + \frac{A_4}{A_0 \left(\dfrac{\partial g}{\partial \bar{\eta}}\right)^2} \frac{\partial W}{\partial \xi} + \frac{A_5}{A_0 \left(\dfrac{\partial g}{\partial \bar{\eta}}\right)^2} \frac{\partial W}{\partial \zeta} = 0 \tag{1}$$

where $\partial g/\partial \bar{\eta}$ and $\partial^2 g/\partial \bar{\eta}^2$ are the first and second derivatives of the stretching function[12] $g(\bar{\eta})$. The quantity W represents $\bar{u}$ in the ξ-momentum equation, w in the ζ-momentum equation, T in the energy equation, and C_i in the species continuity equation. The coefficients A_0 to A_5 are given in Ref. 13.

The remaining first-order PDEs are written as follows:

Global continuity:

$$\frac{\partial}{\partial \xi}(\rho_{sh} u_{sh} \bar{\rho} \bar{u} h_3) - \frac{\bar{\eta}}{n_{sh}} \frac{\partial n_{sh}}{\partial \xi} \frac{\partial}{\partial \eta}(\rho_{sh} u_{sh} \bar{\rho} \bar{u} h_3) \frac{\partial g}{\partial \eta} + \frac{1}{n_{sh}} \frac{\partial}{\partial \eta}(h_1 h_3 \rho_{sh} \bar{\rho} v) \frac{\partial g}{\partial \bar{\eta}} + \frac{\partial}{\partial \zeta}(\rho_{sh} \bar{\rho} w h_1) - \frac{\bar{\eta}}{n_{sh}} \frac{\partial n_{sh}}{\partial \zeta} \frac{\partial}{\partial \eta}(\rho_{sh} \bar{\rho} w h_1) \frac{\partial g}{\partial \bar{\eta}} = 0 \tag{2}$$

η momentum:

$$\frac{\rho_{sh} u_{sh} \bar{\rho} \bar{u}}{h_1} \frac{\partial v}{\partial \xi} + \frac{\rho_{sh} \bar{\rho} v}{n_{sh}} \frac{\partial v}{\partial \eta} \frac{\partial g}{\partial \bar{\eta}} - \frac{\rho_{sh} u_{sh} \bar{\rho} \bar{u} \bar{\eta}}{h_1 n_{sh}} \frac{\partial n_{sh}}{\partial \xi} \frac{\partial v}{\partial \eta} \frac{\partial g}{\partial \bar{\eta}} + \frac{\rho_{sh} \bar{\rho} w}{h_3} \frac{\partial v}{\partial \zeta} - \frac{\rho_{sh} \bar{\rho} w \eta}{h_3 n_{sh}} \frac{\partial n_{sh}}{\partial \zeta} \frac{\partial v}{\partial \eta} \frac{\partial g}{\partial \bar{\eta}} - \frac{\rho_{sh} u_{sh}^2 \bar{\rho} \bar{u}^2}{h_1 n_{sh}} \frac{\partial h_1}{\partial \bar{\eta}} - \frac{\rho_{sh}}{h_3} \frac{\bar{\rho} w^2}{n_{sh}} \frac{\partial h_3}{\partial \bar{\eta}} + \frac{p_{sh}}{n_{sh}} \frac{\partial \bar{p}}{\partial \eta} \frac{\partial g}{\partial \bar{\eta}} = 0 \tag{3}$$

Equation of state:

$$\bar{p} = \bar{\rho} \bar{T} (\bar{\tilde{W}}_{sh} / \bar{\tilde{W}}) \tag{4}$$

Boundary Conditions

The following surface and shock boundary conditions are employed:

Surface Slip Conditions (Employed at $\eta = \eta_s$)

The equations relating the slip values to wall values and gradients at the edge of the Knudsen layer ($\eta = \eta_s$) are[8]

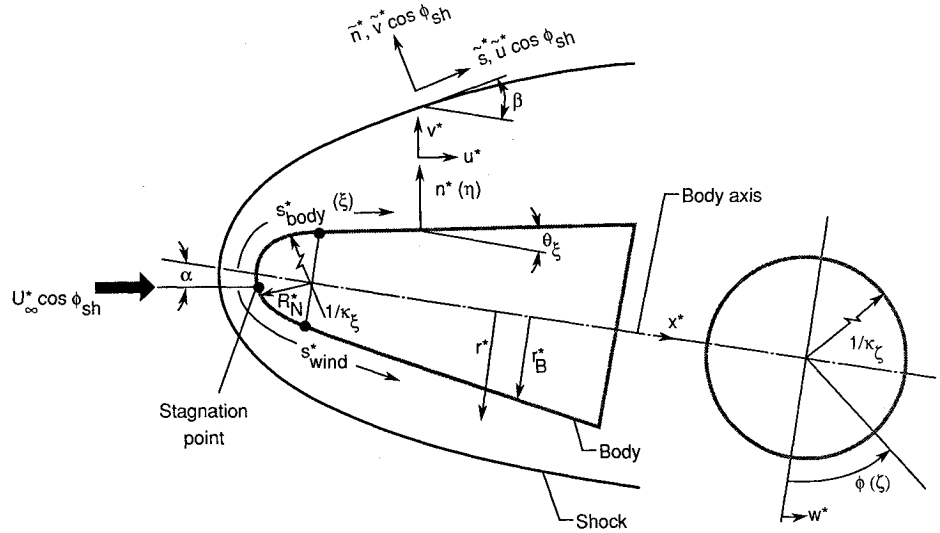

Fig. 1 Body and shock-oriented coordinate systems in a meridional plane.

Tangential velocity slip:

$$\bar{u}_s = \varepsilon^2 \left(1 \Big/ \sum_{i=1}^{NS} \sqrt{\frac{\bar{\bar{W}}}{W_i}}\, C_i^s\right) \left[\sqrt{\frac{\pi}{2}} \left(\frac{2-\theta}{\theta}\right) \frac{\mu_{sh}}{\sqrt{p_{sh}\rho_{sh}}} \frac{\bar{\mu}_s}{\sqrt{\bar{p}_s\bar{\rho}_s}} \times \sqrt{\frac{\bar{\bar{W}}_\infty}{\bar{\bar{W}}_s}} \left(\frac{1}{n_{sh}} \frac{\partial \bar{u}}{\partial \eta} \frac{\partial g}{\partial \bar{\eta}} - \frac{\kappa_\xi \bar{u}}{1 + n_{sh}\bar{\eta}\kappa_\xi}\right)_s\right] \tag{5}$$

Circumferential velocity slip:

$$w_s = \varepsilon^2 \left(1 \Big/ \sum_{i=1}^{NS} \sqrt{\frac{\bar{\bar{W}}_s}{W_i}}\, C_i^s\right) \left[\sqrt{\frac{\pi}{2}} \left(\frac{2-\theta}{\theta}\right) \frac{\mu_{sh}}{\sqrt{p_{sh}\rho_{sh}}} \frac{\bar{\mu}_s}{\sqrt{\bar{p}_s\bar{\rho}_s}} \times \sqrt{\frac{\bar{\bar{W}}_\infty}{\bar{\bar{W}}_s}} \left(\frac{1}{n_{sh}} \frac{\partial \bar{u}}{\partial \eta} \frac{\partial g}{\partial \bar{\eta}} - \frac{\kappa_\zeta w \cos\theta_\xi}{1 + \kappa_\zeta n_{sh}\bar{\eta}\cos\theta_\xi}\right)_s\right] \tag{6}$$

Temperature slip (with frozen internal energy during reflection from surface):

$$T_s = T_w + \frac{1}{2}\sqrt{\frac{\pi}{2}} \left(\frac{2-\theta}{\theta}\right) \left(\frac{\bar{\gamma}}{\bar{\gamma}-1}\right)_s \varepsilon^2 \frac{\mu_{sh}}{n_{sh}\overline{Pr}Pr_{sh}\sqrt{p_{sh}\rho_{sh}}} \times \frac{\bar{\mu}_s}{\sqrt{\bar{p}_s\bar{\rho}_s}} \left[1 \Big/ \sum_{i=1}^{NS} \left(\frac{\bar{\bar{W}}_s}{W_i}\right)^{3/2} C_i^s\right] \left(\frac{\partial T}{\partial \eta} \frac{\partial g}{\partial \bar{\eta}}\right)_s + \varepsilon^2 \sqrt{\frac{\pi}{2}} \frac{\mu_{sh} Le_{sh} \overline{Le}_s}{n_{sh} Pr_{sh} \sqrt{p_{sh}\rho_{sh}} \overline{Pr}} \frac{\bar{\mu}_s}{\sqrt{\bar{p}_s\bar{\rho}_s}} \left[1 \Big/ \sum_{i=1}^{NS} \left(\frac{\bar{\bar{W}}_s}{W_i}\right)^{3/2} C_i^s\right] \times \left(\frac{5}{4}\frac{2-\theta}{\theta} T_s + T_w\right) \sum_{i=1}^{NS} \left[\frac{\partial C_i}{\partial \eta} \frac{\partial g}{\partial \bar{\eta}} - (1 - C_i) \sum_{q=1}^{NS} \left(\frac{\bar{\bar{W}}_s}{W_q}\right) \frac{\partial C_q}{\partial \eta} \frac{\partial g}{\partial \bar{\eta}}\right]_s \tag{7}$$

Pressure slip:

$$\bar{p}_s = \bar{p}_w + \frac{4}{5\sqrt{2\pi}} \left(\frac{2-\theta}{\theta}\right) \left(\frac{\bar{\gamma}}{\bar{\gamma}-1}\right)_s \varepsilon^2 \frac{1}{n_{sh} Pr_{sh} \overline{Pr}_s \sqrt{p_{sh}\rho_{sh}}} \times \sqrt{\frac{\bar{p}_s}{\bar{\rho}_s}} \left(\frac{1}{T} \frac{\partial T}{\partial \eta} \frac{\partial g}{\partial \bar{\eta}}\right)_s \sum_{i=1}^{NS} \left(\frac{\bar{\bar{W}}_s}{W_i}\right)^{3/2} C_i \bar{\mu}_i^s \mu_{sh} \tag{8}$$

Concentration slip:

$$C_i^w = C_i^s \left(\frac{\bar{\rho}_s}{\bar{\rho}_w}\right) \sqrt{\frac{T_s}{T_w}} + \varepsilon^2 \sqrt{\frac{\pi}{2T_w}} \left(\frac{\mu_{sh} Le_{sh}}{Pr_{sh}}\right) \left(\frac{\overline{Le}\bar{\mu}}{\overline{Pr}}\right)_s \times \frac{1}{\sqrt{p_{sh}\rho_{sh}}} \sqrt{\frac{T_s}{\bar{p}_{sh}\bar{\rho}_s}} \left(\frac{\bar{\rho}_s}{\bar{\rho}_w}\right) \left(\frac{W_i}{\bar{\bar{W}}_s}\right)^{3/2} \times \left[\frac{1}{n_{sh}} \frac{\partial C_i}{\partial \eta} \frac{\partial g}{\partial \bar{\eta}} + \frac{(1 - C_i)}{n_{sh}} \sum_{q=1}^{NS} \frac{\bar{\bar{W}}_s}{W_q} \frac{\partial C_q}{\partial \eta} \frac{\partial g}{\partial \bar{\eta}}\right]_s \tag{9a}$$

where

$$C_i^s = 1 + \left[\left(\frac{\partial C_i}{\partial \eta} \frac{\partial g}{\partial \bar{\eta}}\right)_s + \frac{W_A}{W_i} n_{sh} \psi_i^s\right] \Big/ \sum_{q=1}^{NS} \left(\frac{\bar{\bar{W}}}{W_q} \frac{\partial C_q}{\partial \eta} \frac{\partial g}{\partial \bar{\eta}}\right)_s \tag{9b}$$

with

$$A = \mathrm{O} \quad \text{for} \quad i = \mathrm{O}_2 \quad \text{and} \quad A = \mathrm{N} \quad \text{for} \quad i = \mathrm{N}_2 \tag{9c}$$

$$\psi_A^s = -\frac{1}{\varepsilon^2} \sqrt{\frac{2}{\pi}} \left(\frac{\gamma_A}{2 - \gamma_A}\right)_s \frac{\sqrt{p_{sh}\rho_{sh}}}{\mu_{sh}} \frac{Pr_{sh}\overline{Pr}_s}{\overline{Le}_s Le_{sh}} \times \frac{\sqrt{\bar{p}_s\bar{\rho}_s}}{\bar{\mu}_s} \left(\frac{\bar{\bar{W}}_s}{W_A}\right)^{3/2} C_A^s, \qquad (A = \mathrm{O}, \mathrm{N}) \tag{9d}$$

$$\psi_M^s = -\psi_A^s, \qquad \begin{pmatrix} A = \mathrm{O} & \text{for} & M = \mathrm{O}_2 \\ A = \mathrm{N} & \text{for} & M = \mathrm{N}_2 \end{pmatrix} \tag{9e}$$

$$\psi_i^s = 0, \qquad \text{(for all other species)} \tag{9f}$$

In Eqs. (9b), (9d), and (9e), the subscript A denotes an atomic species O or N.

For noncatalytic surface, $\gamma_A = 0$ in Eq. (9d), and Eq. (9b) with $\psi_i = 0$ for all the species, gives[8]

$$\frac{\partial C_i}{\partial \eta} = 0 \tag{10}$$

For a fully catalytic surface at sufficiently low temperatures, an appropriate boundary condition is

$$(C_i)_s = (C_i)_\infty \tag{11}$$

Shock-Slip Conditions (employed at $\eta = 1$):

Continuity:

$$\rho_{sh}\tilde{v}_{sh} = -\sin\beta \tag{12}$$

$\tilde{s}$ momentum:

$$\varepsilon^2\mu_{sh}\left\{\frac{1}{n_{sh}}\left[\cos(\beta-\theta_\xi)+\frac{\partial n_{sh}}{\partial\xi}\sin(\beta-\theta_\xi)\right]\left(\frac{\partial g}{\partial\bar{\eta}}\frac{\partial\tilde{u}}{\partial\eta}\right)_{sh} - \left(\frac{\partial\tilde{u}}{\partial\xi}\right)_{sh}\sin(\beta-\theta_\xi)\right\} + \sin\beta\tilde{u}_{sh} = \cos\beta\sin\beta \tag{13a}$$

where

$$\left(\frac{\partial\tilde{u}}{\partial\eta}\right)_{sh} = \left[\left(\frac{\partial u}{\partial\eta}\right)_{sh}\cos(\beta-\theta_\xi) + \left(\frac{\partial v}{\partial\eta}\right)_{sh}\sin(\beta-\theta_\xi)\right]\Big/\cos\phi_{sh} \tag{13b}$$

$$\left(\frac{\partial\tilde{u}}{\partial\xi}\right)_{sh} = \left[\left(\frac{\partial u_{sh}}{\partial\xi}\right)_{sh}\cos(\beta-\theta_\xi) + \left(\frac{\partial v}{\partial\xi}\right)_{sh}\sin(\beta-\theta_\xi)\right]\Big/\cos\phi_{sh} \tag{13c}$$

$\tilde{n}$ momentum:

$$p_{sh} = p_\infty + \sin\beta(\sin\beta + \tilde{v}_{sh}) + \varepsilon^2\frac{4}{3}\left(\mu\frac{\partial\tilde{v}}{\partial\tilde{n}}\right)_{sh} \tag{14}$$

Energy:

$$\frac{\varepsilon^2K_{sh}}{\sin\beta}\left\{\frac{1}{n_{sh}}\left[\cos(\beta-\theta_\xi)+\frac{\partial n_{sh}}{\partial\xi}\sin(\beta-\theta_\xi)\right]\left(\frac{\partial T}{\partial\eta}\frac{\partial g}{\partial\bar{\eta}}\right)_{sh} - \left(\frac{\partial T}{\partial\xi}\right)_{sh}\sin(\beta-\theta_\xi)\right\} + \sum_{i=1}^{NS}C_{i,sh}h_{i,sh} - \frac{1}{2}[(\tilde{u}_{sh}-\cos\beta)^2 + (\sin^2\beta - \tilde{v}_{sh}^2)] + \frac{\varepsilon^2}{\sin\beta}\frac{\mu_{sh}}{Pr_{sh}} \times \sum_{i=1}^{NS}Le_{i,sh}h_{i,sh}\left\{\frac{1}{n_{sh}}\left[\cos(\beta-\theta_\xi) + \frac{\partial n_{sh}}{\partial\xi}\sin(\beta-\theta_\xi)\right]\left(\frac{\partial C_i}{\partial\eta}\frac{\partial g}{\partial\bar{\eta}}\right)_{sh} - \left(\frac{\partial C_i}{\partial\xi}\right)_{sh}\sin(\beta-\theta_\xi)\right\} = \sum_{i=1}^{NS}C_{i,\infty}h_{i,\infty} + \frac{\varepsilon^2}{\sin\beta}\left[\frac{4}{3}\mu\frac{\partial}{\partial\tilde{n}}(\tilde{v}^2)\right]_{sh} \tag{15}$$

Species continuity:

$$\frac{\varepsilon^2\mu_{sh}Le_{i,sh}}{Pr_{sh}}\left\{\frac{1}{n_{sh}}\left[\cos(\beta-\theta_\xi)+\frac{\partial n_{sh}}{\partial\xi}\sin(\beta-\theta_\xi)\right] \times \left(\frac{\partial C_i}{\partial\eta}\frac{\partial g}{\partial\bar{\eta}}\right)_{sh} - \left(\frac{\partial C_i}{\partial\xi}\right)_{sh}\sin(\beta-\theta_\xi)\right\} + \sin\beta(C_{i,sh}-C_{i,\infty}) = \int_{sh}^{\infty}\dot{w}_i\,d\eta = \dot{w}_{i,av}\delta_{sh} \tag{16a}$$

with

$$\dot{w}_{i,av} = \dot{w}_{i,sh}/2 \tag{16b}$$

$$\delta_{sh} = (\eta_\infty - \eta_{sh}) \tag{16c}$$

The shock thickness δ_{sh} to a good degree of approximation may be obtained from

$$\delta_{sh} = 0.174M_\infty\varepsilon^2 \tag{16d}$$

Equation (16d) has been approximated from Refs. 14 and 15. This equation has been further verified by integrating the equations for a merged stagnation shock layer of nonequilibrium dissociating gas[16] with the same properties as those used here. The shock thickness δ_{sh}, obtained in Ref. 16 from integrating through the shock, keeping the $\dot{w}_i$ term, is very close to that obtained from Eq. (16d). The importance of keeping the production term $\dot{w}_i$ in the shock transition zone (or, alternatively in the shock-slip relations) is shown in Ref. 16. If the shock is thin (i.e., δ_{sh} is of order 10^{-2}) the mass rate of production of atoms $\dot{w}_i$ may be assumed negligible across the shock. This assumption makes the right-hand side of Eq. (16a) zero.

Since velocity components tangent and normal to the shock (see Fig. 1) are not the same as those tangent and normal to the body, the following transformations are needed to obtain velocity components at the shock in the body-oriented coordinates from the shock-oriented coordinates:

$$u_{sh} = \tilde{u}_{sh}\cos\phi_{sh}\cos(\beta-\theta_\xi) - \tilde{v}_{sh}\cos\phi_{sh}\sin(\beta-\theta_\xi) \tag{17}$$

$$v_{sh} = \tilde{u}_{sh}\cos\phi_{sh}\sin(\beta-\theta_\xi) + \tilde{v}_{sh}\cos\phi_{sh}\cos(\beta-\theta_\xi) \tag{18}$$

$$w_{sh} = -\sin\phi_{sh}\sqrt{\tilde{u}_{sh}^2 + \tilde{v}_{sh}^2} \tag{19}$$

where β and θ_ξ are the shock and body angles, respectively, and ϕ_{sh} is the crossflow angle (see Fig. 2a) defined as[17]

$$\sin\phi_{sh} = w/U_\infty = -\sin(\sigma' - \theta_2')N_\phi + \cos(\sigma' - \theta_2')T_\phi \tag{20}$$

In Eq. (20), $(\sigma' - \theta_2')$ is the angle that the velocity vector after crossing the shock makes with the shock-tangent vector $\hat{T}$ in the $\hat{N} - \hat{T}$ plane (see Fig. 2b), and N_ϕ and T_ϕ are the components of normal and tangential vectors $\hat{N}$ and $\hat{T}$, respectively, in the crossflow direction (see Fig. 2a). For a two-dimensional flow over an axisymmetric body at zero degree angle of attack, Eqs. (17) and (18) reduce to those given in Ref. 18 with $\phi_{sh} = 0$ deg.

Alternately, the following relations can also be used to relate the velocity components at the shock in the body- and shock-oriented coordinate systems:

$$u_{sh} = \cos\phi_{sh}\cos(\beta_{sh} - \theta_\xi)\sqrt{\tilde{u}_{sh}^2 + \tilde{v}_{sh}^2} \tag{21}$$

$$v_{sh} = \cos\phi_{sh}\sin(\beta_{sh} - \theta_\xi)\sqrt{\tilde{u}_{sh}^2 + \tilde{v}_{sh}^2} \tag{22}$$

$$w_{sh} = -\sin\phi_{sh}\sqrt{\tilde{u}_{sh}^2 + \tilde{v}_{sh}^2} \tag{23}$$

where β_{sh} is the flow angle from the body axis in a meridional (or ϕ = const) plane[17] (see Fig. 2c),

$$\tan\beta_{sh} = \frac{-\sin(\sigma' - \theta_2')N_r + \cos(\sigma' - \theta_2')T_r}{-\sin(\sigma' - \theta_2')N_x + \cos(\sigma' - \theta_2')T_x} \tag{24}$$

with angles σ' and θ_2' defined in Fig. 2b and N_x, T_x and N_r, T_r are the components of vectors $\hat{N}$ and $\hat{T}$ in the body-axis and radial directions, respectively.

Angle $(\beta_{sh} - \theta_\xi)$ appearing in Eqs. (21) and (22) may be obtained from (see Fig. 2c):

$$\tan(\beta_{sh} - \theta_\xi) = v_{sh}^*/u_{sh}^* = v_{sh}/u_{sh} \tag{25}$$

Chemical Reaction Model

The net mass rate of production of a chemical species per unit volume $\dot{w}_i^*$ is obtained from the usual kinetic relations.[19]

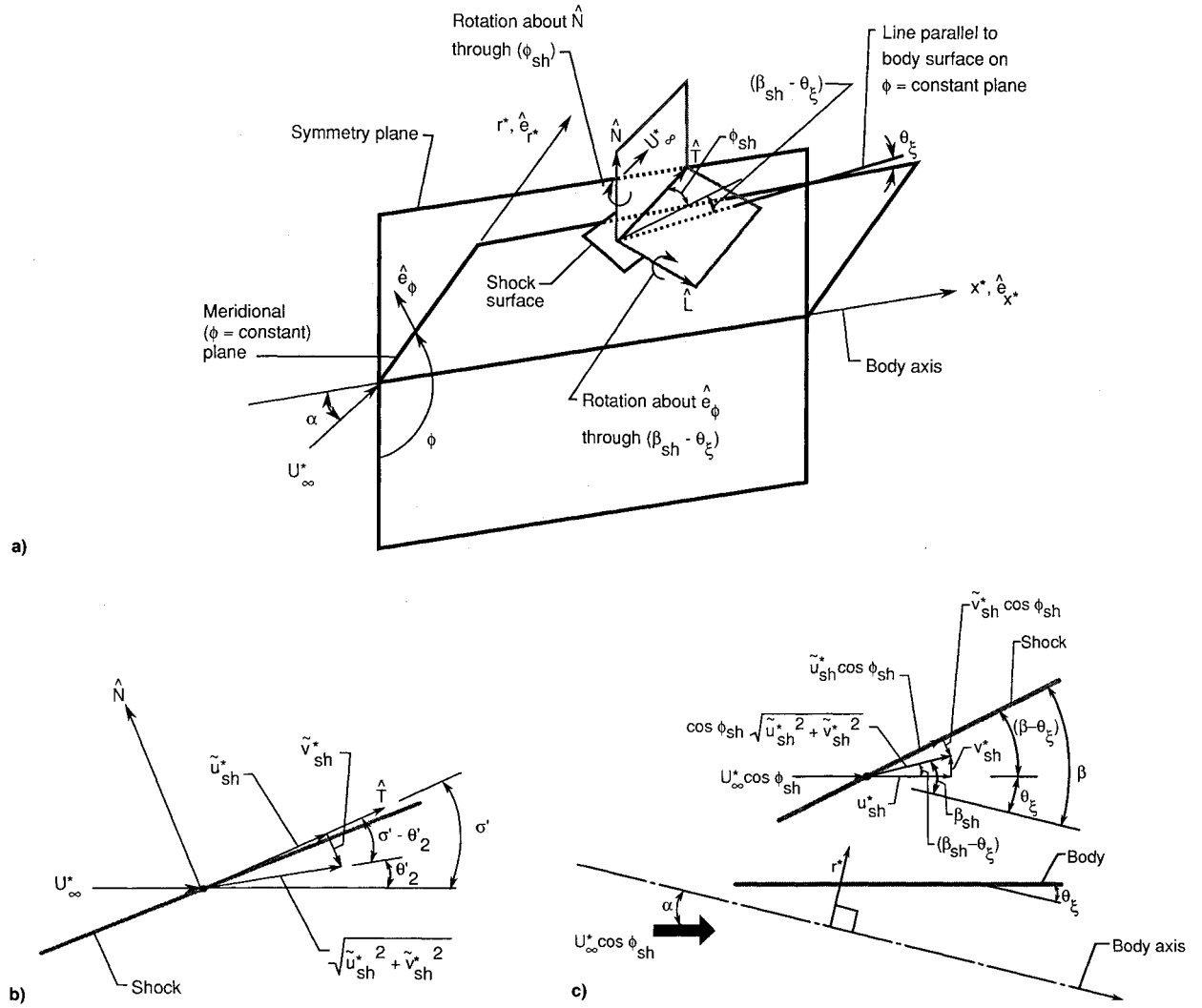

Fig. 2 Shock-wave vectors, rotation angles, shock and flow angles, and velocity components for shock boundary conditions: a) shock-wave normal and tangent vectors and rotation angles about $\hat{N}$ and $\hat{e}_\phi$ vectors, b) shock and flow angles in the $\hat{N} - \hat{T}$ plane, and c) velocity components and angles in a meridional (ϕ = const) plane.

For the seven species (O_2, N_2, O, N, NO, NO^+, and e^-) air calculations in the present code, the reaction model is similar to that used in Ref. 19. The species production terms appearing in the energy and species continuity equations are written in terms of temperature and concentration following the approach of Ref. 19. The reaction rate constants and the relative efficiencies of the catalytic third bodies are obtained from Ref. 19. These rate constants and the catalytic efficiencies are identical to those reported in Ref. 20 for the seven-species air model up to a temperature of about 12,000 K.

Thermodynamic and Transport Properties

Thermodynamic properties for the multicomponent air mixture obtained by assuming a thermally perfect gas and for the individual species are obtained from Ref. 20.

Transport properties for the gas mixture are obtained using the methods of Ref. 21 for viscosity and that of Ref. 22 for thermal conductivity. Individual species viscosity and frozen thermal conductivity are based on the work of Ref. 20.

In this study, a variable Prandtl number is used, whereas the Lewis number is set equal to 1.4. For the ionized species, an ambipolar type of diffusion is employed.[23] For such a diffusion the binary diffusion coefficients must be doubled in the calculations. Accordingly, a Lewis number of 2.8 has been used for the ionized species. Previous studies[5,6,9] ignored this effect.

Method of Solution

Murray and Lewis[24] presented a method for solving the three-dimensional, perfect gas viscous-shock-layer equations along a body. Reference 9 applied this method of solution to three-dimensional nonequilibrium flows. A similar finite difference method is used here to solve the ξ momentum, ζ momentum, energy, and species continuity equations. By using two-point backward differences in the ξ direction, the zig-zag finite difference expressions of Krause[25] in the ζ direction, and central differences in the η direction in the second-order parabolic Eq. (1), a tridiagonal finite difference form is obtained that can be solved by the Thomas algorithm for each dependent variable represented by W. The solution of this second-order set of equations is obtained by an uncoupled cascading scheme. The first-order PDEs, Eqs. (2) and (3) of continuity and normal momentum, respectively, are solved by a similar method, but they are coupled together.[24] The coupled solution of these two equations promotes convergence and ensures stability in the marching solution, especially for the slender bodies.[12]

There are a few points in the flowfield where the governing equations become singular, and the limiting form must be evaluated. Along the stagnation streamline, the ξ derivatives of the pressure and shock standoff distance are zero, and the tangential component of velocity behind the shock u_{sh} is also zero. These zero values result in a singularity in the coefficients of

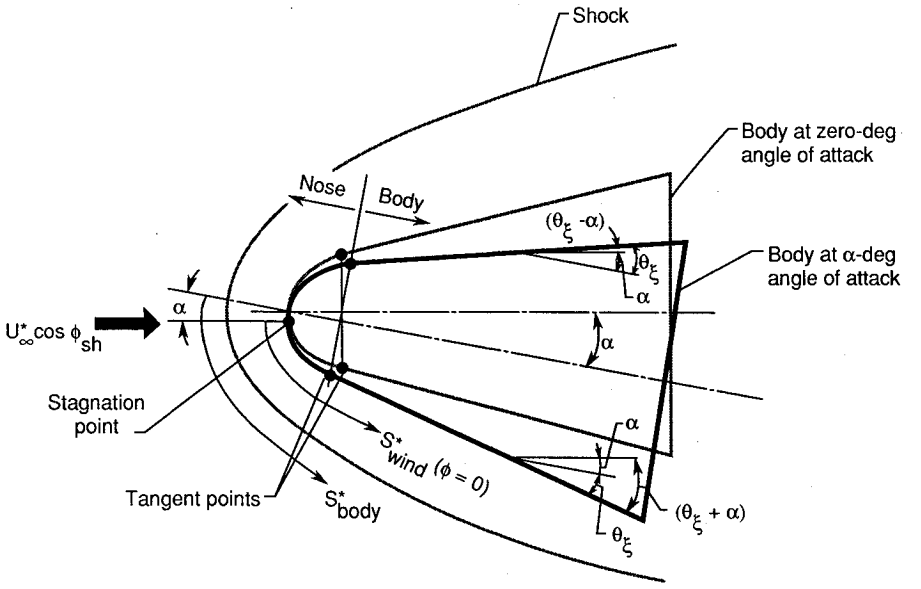

Fig. 3 Coordinates and bodies at zero and α-deg angles of attack.

the ξ-momentum equation. The continuity equation also becomes singular with ξ approaching zero. These singularities are removed by using the series expansions of Ref. 24. Further, the crossflow velocity w is zero along the windward and leeward streamlines, and the value of $\partial w/\partial \zeta$ is needed in the continuity equation. This is obtained by taking the ζ derivative of the crossflow equation and solving for the new dependent variable $\partial w/\partial \zeta$. In the windward and leeward planes, the ζ derivatives of all dependent variables, except that of w, are zero, and the second derivative of w is zero. The equation of $\partial w/\partial \zeta$ is solved by writing it in the standard parabolic form, namely, Eq. (1).

The solution begins on the spherical nosecap at the aerodynamic stagnation point where an axisymmetric solution in a wind-fixed coordinate system is obtained. The axisymmetric (one-plane) solution on the sphere is marched downstream to encompass the aerodynamic and geometric stagnation points. The wind-fixed solution is then rotated around the sphere and interpolated to obtain the shock-layer profiles in the body-fixed (three-dimensional) coordinate system. These are used as the initial profiles for the three-dimensional solution. The three-dimensional solution begins in the windward plane at a specified streamwise (or ξ) location and marches around the body obtaining a converged solution at each circumferential (or ζ direction) step. The governing equations are solved at each point in the flowfield in the following order: species continuity, crossflow (or ζ) momentum, energy, streamwise momentum, integration of global continuity for shock standoff distance n_{sh}, and the coupled normal (or η) momentum and continuity equations. After integration of the continuity equation, the new shock standoff distance is used to update the shock-layer profiles for the next local iteration while the shock slope, $\partial n_{sh}/\partial \xi$, remains fixed at the input value. The equations are iterated in this manner until each of the flowfield variables is converged through the entire shock layer at the given ξ and ζ stations. Global convergence of the VSL solutions is satisfied by repeating the calculations over the entire body using the computed shock standoff distance obtained from the previous pass to provide the new shock shape (i.e., shock standoff distance and its slope). Global iterations are repeated until the input and output shock shapes are converged. Other details of the solution procedure are provided in Ref. 13.

Calculation of Input Shock Shape

The global iteration process outlined in the previous paragraph requires an initial value of the shock slope, $\partial n_{sh}/\partial \xi$, and $\partial v/\partial \xi$, which introduces an elliptic effect into the equations. In the present scheme, $\partial n_{sh}/\partial \xi$ is obtained either from an inviscid equilibrium air solution[26] (which is scaled by a constant), or from a viscous nonequilibrium analysis. The values of $\partial v/\partial \xi$ are calculated from a backward-difference approximation. The scaling factor used with the inviscid equilibrium solution for the shock standoff distance is in the range of 1.2–1.25. The initial input shock shape obtained from this scaling accounts for the nonequilibrium effects on the flowfield and limits the shock-shape correction and, therefore, decreases the required global iterations.

Even though the results obtained from using an inviscid equilibrium shock shape with a scaling factor are satisfactory for nonequilibrium viscous flows at high Reynolds numbers, convergence problems are encountered at freestream Reynolds numbers (based on the nose radius) less than about 2000. These values of the Reynolds number are encountered under the low-density flight conditions. Under these conditions, the entire shock layer becomes viscous. An alternate method for obtaining a three-dimensional viscous, nonequilibrium input shock shape is, therefore, suggested here. The starting point is the generation of a two-dimensional viscous nonequilibrium shock shape for an axisymmetric body (see Fig. 3) with effective angles of $(\theta_\xi + \alpha)$ (for simulating the flowfield on the windward side) and $(\theta_\xi - \alpha)$ (for simulating the flowfield on the leeward side). The two-dimensional solutions can be obtained from the three-dimensional VSL code by running it in the two-dimensional mode. For the body at α, these solutions are used from the aerodynamic stagnation point up to the tangency point (where the nose of the body is axisymmetric) in the wind-fixed coordinates (see Fig. 3). Beyond the tangency point, the shock shape (for the body solutions) is specified in the body-fixed coordinates. The relationship between the wind-fixed and body-fixed coordinates (shown in Figs. 1 and 3) along the windward and leeward streamlines, respectively, is

$$(s^*_{wind})_{\zeta(\phi)=0} = s^*_{body} - \alpha \tag{26a}$$

$$(s^*_{wind})_{\zeta(\phi)=\pi} = s^*_{body} + \alpha \tag{26b}$$

Having obtained the windward- and leeward-side values of the shock standoff distance and shock slope from the two-dimensional solutions of bodies with effective body angles, their distributions around the body $[0 \leq \zeta(\phi) \leq \pi]$ for body solution (i.e., beyond the tangency point) may be obtained from

$$(n^*_{sh})_{(s^*_{body})_{TP}} = [(n^*_{sh})_{\theta_\xi+\alpha}]_{(s^*_{body})_{TP}-\alpha}[(1 + \cos \phi)/2] + [(n^*_{sh})_{\theta_\xi-\alpha}]_{(s^*_{body})_{TP}+\alpha}[(1 - \cos \phi)/2] \tag{27}$$

$$\left[\frac{\partial n_{sh}^*}{\partial s^*}\right]_{(s^*_{body})_{TP}} = \left[\left(\frac{\partial n_{sh}^*}{\partial s^*}\right)_{\theta_\xi+\alpha}\right]_{(s^*_{body})_{TP}-\alpha}\left(\frac{1+\cos\phi}{2}\right) + \left[\left(\frac{\partial n_{sh}^*}{\partial s^*}\right)_{\theta_\xi-\alpha}\right]_{(s^*_{body})_{TP}+\alpha}\left(\frac{1-\cos\phi}{2}\right) \quad (28)$$

The same relations are valid for $s^*_{body} > (s^*_{body})_{TP}$.

Results and Discussion

Detailed flowfield results have been obtained for hypersonic, low-density, two- and three-dimensional, nonequilibrium viscous shock-layer flows. Three-dimensional calculations are performed for sphere–cone-shaped bodies at various angles of attack. Obtained results show the effect of low density on the flowfield around hypervelocity vehicles. Present predictions have been compared with the available experimental data and other numerical predictions, including those from the DSMC method.

Results for Nonequilibrium Flow Without Slip

These results have been obtained to check the accuracy of the solutions with the new grid and transport properties, as well as to study the effect of input shock shape. As mentioned earlier, the input shock plays a major role in obtaining good quality solutions and their global convergence.

Effect of Input Shock Shape

Figure 4 shows the input shock shapes for the leeward and windward sides obtained from the inviscid equilibrium and viscous nonequilibrium flowfield calculations. As mentioned earlier, the inviscid equilibrium shock shape is obtained from the code of Ref. 26. The viscous nonequilibrium shock shape is obtained from two-dimensional calculations using the effective body angles for the windward and leeward sides and employing a cosine distribution to obtain shock shapes for other meridional planes. As expected, the shock standoff distance obtained from the inviscid equilibrium calculations is smaller than the one obtained from the viscous nonequilibrium computations. The difference between the two values increases with the decrease in density, especially on the leeward side. Figure 5 gives the same shock standoff distance by employing the two different shock shapes of Fig. 4 for this relatively high Reynolds number case. Surface heat transfer coefficient employing the two input shock shapes converges to almost the same value as shown in Fig. 6, with inviscid equilibrium input shock shape requiring an additional global pass for this case. For moderately high Reynolds number nonequilibrium flowfield calculations, an input shock shape obtained from inviscid equilibrium flow calculations serves as a good initial guess with a scaling factor of about 1.2. However, for the fairly low Reynolds number flows ($Re_\infty \leq 2000$), solutions may never converge with an inviscid equilibrium input shock shape.[13] No such convergence problems are encountered with a rotated input shock shape.[13]

Effect of Angle of Attack

The surface heat transfer coefficient for a 9-deg sphere cone at three different angles of attack (5, 8, and 11 deg) is given in Fig. 7. The results are shown only for the leeward and windward meridional planes. As before, the axisymmetric results for the spherical nose are given in wind-fixed coordinates, whereas the three-dimensional results beyond the tangency point are given in body-fixed coordinates. The heating at the aerodynamic stagnation point increases with increase in α and the maximum value is obtained for $\alpha = 11$ deg. This increase in heating is because of the increased shock-shape asymmetry for larger values of α (e.g., see Fig. 3). Also, the heating is highest for the windward side, and lowest for the leeward side of the body at 11-deg angle of attack than at lower angles of attack.

Comparison with Two-Dimensional Results

Detailed comparisons of the results obtained for a 20-deg sphere cone at 0-deg angle of attack by employing the present three-dimensional nonequilibrium viscous-shock-layer code and a two-dimensional nonequilibrium viscous-shock-layer code[27] are provided in Ref. 13. Both of these codes employ similar computational grids, reaction-rate kinetics, transport, and thermodynamic properties. Therefore, the two codes predict, as expected, almost the same velocity, temperature, and species concentration profiles.[13]

Results for Nonequilibrium Flow with Slip

Comparison with Experimental Data

Before carrying out nonequilibrium calculations for the low-density (or low Reynolds number) flows, RAM C-II and RAM C-III (Refs. 28 and 29) flight data were used to verify the accuracy of predictions obtained from the present three-dimensional nonequilibrium viscous shock-layer (VSL3DNQ) code with slip. These (RAM C-II and RAM C-III) were two of the three Radio Attenuation Measurement test vehicles for the investigation of flowfield plasma under re-entry conditions. The basic vehicle was a 9-deg spherically blunted cone and was instrumented to measure electron number density across the shock layer. Microwave reflectometers were used to measure the peak values of electron number

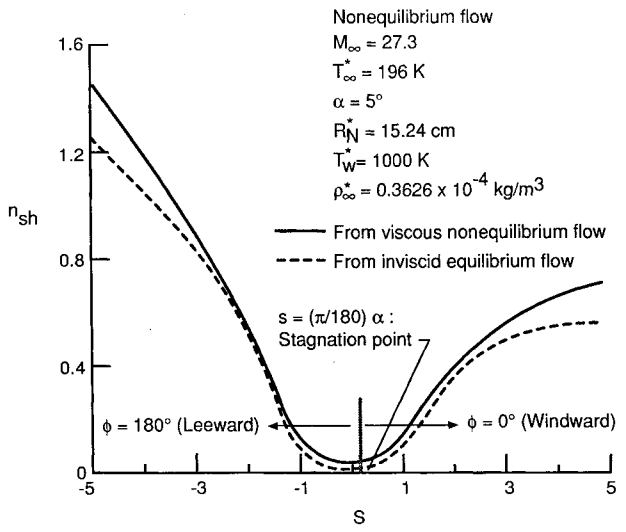

Fig. 4 Comparison of input shock-layer thickness for a 9-deg sphere–cone from two approaches.

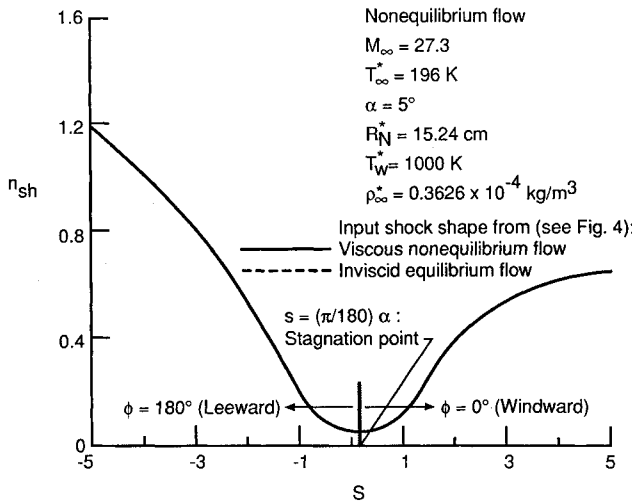

Fig. 5 Comparison of output shock-layer thickness for a 9-deg sphere–cone from two approaches.

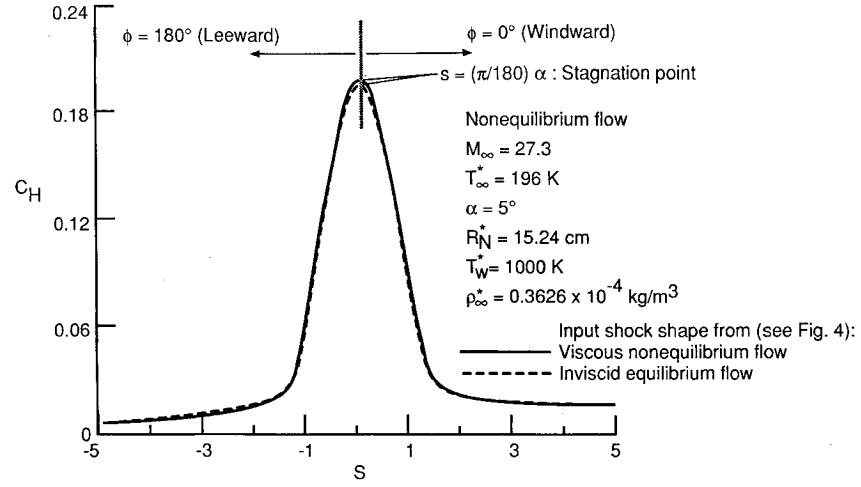

Fig. 6 Comparison of heat transfer coefficient for a 9-deg sphere–cone from two input shock shapes.

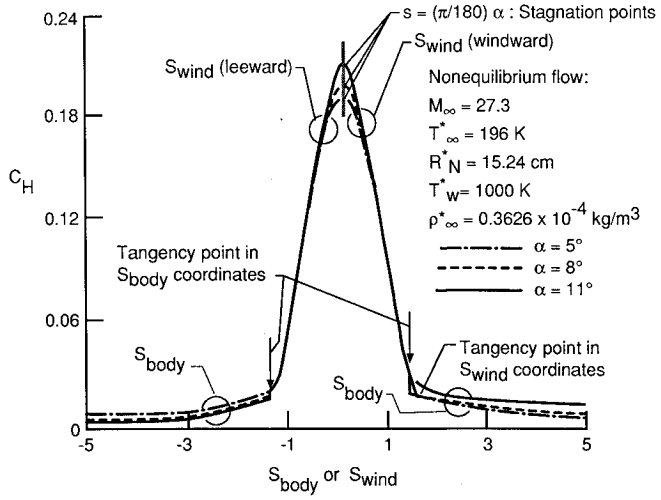

Fig. 7 Comparison of heat transfer coefficient for a 9-deg sphere–cone at different angles of attack.

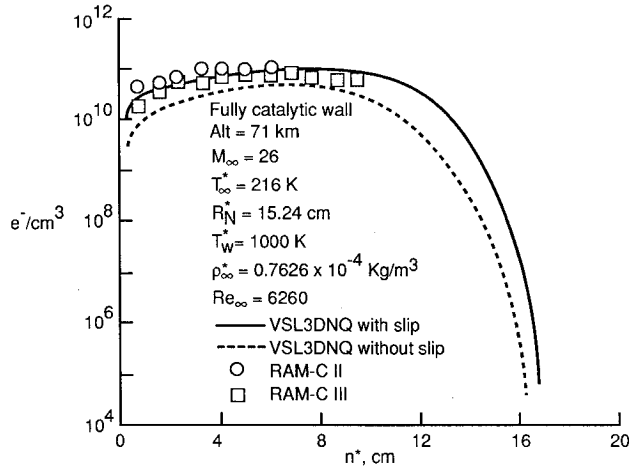

Fig. 8 Predicted and experimental profiles of electron density across the shock layer for RAM-C conditions.

densities in the shock layer at several locations along the cone. A langmuir probe rake that extended across the shock layer at the base of the cone measured electron number density profiles. Details of the vehicle and experiment are given in Refs. 28 and 29. RAM C flight data are few of the data available for the flowfield profiles under the high-energy, low-density flight conditions. Figure 8 shows a comparison of the flight-data and the present predictions with and without surface and shock slip. Present results have been obtained for a fully catalytic surface at a constant wall temperature of 1000 K, using a seven-species chemistry model. A good agreement is obtained between the data and the predictions with the slip conditions. With shock slip, a greater degree of dissociation and ionization is obtained behind the shock. This gives a larger electron density distribution through the shock layer as compared to the no-slip case. The present predictions of peak electron number density within the shock layer compare very well with the experimental data, as shown in Fig. 9. Similar to Fig. 8, the no-slip values are lower because of the reduced levels of dissociation and ionization behind the shock. These comparisons show that the accuracy of the low-density predictions with the present slip-formulation is quite good.

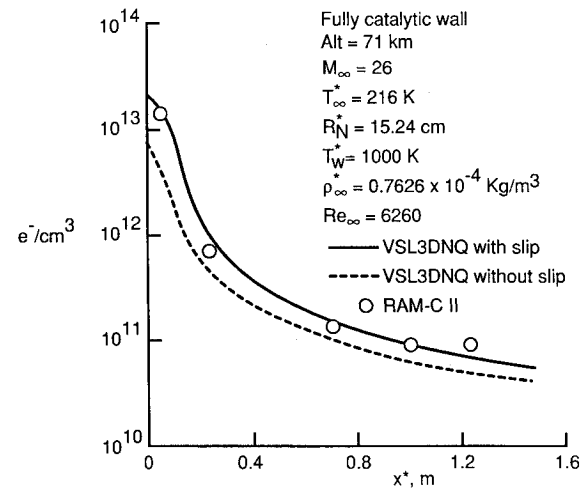

Fig. 9 Comparison of predicted peak electron density with experimental data for RAM-C II flight vehicle.

Comparisons with DSMC and Other Calculations

Figure 10 gives a comparison between the present predictions and those of Ref. 30 from the DSMC method. Present results are shown with and without the surface and shock-slip boundary conditions. These predictions are based on the surface and shock-slip conditions presented here and the computational grid of Ref. 12. The results without corrections are those obtained from the code of Ref. 9 with slip formulation of Ref. 7. These results are used in Ref. 30 for comparison with the DSMC predictions. Clearly, the present VSL3DNQ-slip predictions (with corrections) are in better

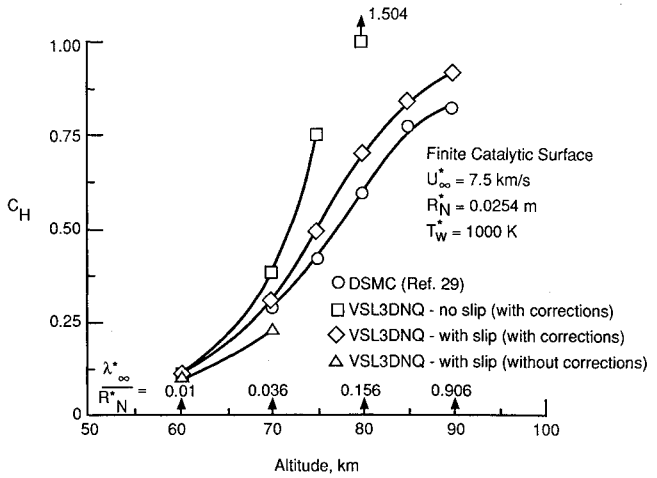

Fig. 10 Predicted stagnation-point heat transfer coefficient at different altitudes.

agreement with the DSMC results and have similar behavior at high altitudes. The differences between two results may be because of the surface interaction models, the transport properties, and the computational grid employed in the calculations. Present predictions as well as the DSMC results approach the no-slip VSL predictions under the high-density flow conditions, as expected. Substantial computer resources (both computational time and storage) are required to obtain the DSMC results, especially at moderately high densities such as those shown between 60 and 75 km altitudes in Fig. 10. Finally, Fig. 10 shows that the viscous shock-layer equations with the present slip conditions give results comparable to the DSMC calculations (considered adequate for the low-density flows) up to a freestream Knudsen number (λ^*_∞/R^*_N) of about unity. Therefore, this formulation can be considered sufficient and fairly accurate for Knudsen number values of less than 1.

Concluding Remarks

Results from this study are summarized as follows:

1) A three-dimensional viscous-shock-layer (VSL3DNQ) code has been modified for analyzing the low-density, nonequilibrium flow past hypervelocity vehicles. This code is robust, dependable, and fairly accurate. Applications, however, are limited to axisymmetric configurations.

2) Recently obtained surface and shock-slip boundary conditions are implemented to account for the low-density effects.

3) The governing equations are solved in the computational domain with a uniform grid. The grid-transformation employed gives finer resolution at both surface and shock and does not add any numerical dissipation to the results.

4) Input shock shape obtained from viscous nonequilibrium flow results in a superior convergence history, especially for the low-density flows.

5) Excellent agreement is obtained with the RAM C flight data for the low-density, high-energy flow conditions.

6) Present results compare favorably with those obtained from the DSMC method for the low-density hypersonic flows.

Finally, despite its certain limitations, the viscous shock-layer method has been shown to be computationally efficient and a valuable tool for analyzing the low-density flows. With the method suggested here for obtaining the input shock shape for the three-dimensional nonequilibrium viscous flows, the VSL method becomes self-starting, unlike the parabolized Navier–Stokes (PNS) methods. The VSL method has been used for obtaining starting profiles for some PNS calculations. The surface-slip conditions presented here may also be used for low-density calculations employing the Navier–Stokes equations. Further, if a shock-fitting approach is used for such calculations to keep the computer storage requirement reasonably small, the present shock-slip formulation can be utilized.

Acknowledgments

The author expresses his appreciation to S. Nayani for assistance in obtaining the results reported here and in preparation of the manuscript, and he also thanks R. A. Thompson for helpful discussions at various stages of this work.

References

[1]Gupta, R. N., Lee, K. P., and Zoby, E. V., "Enhancements to Viscous-Shock-Layer Technique," *Journal of Spacecraft and Rockets*, Vol. 30, No. 4, 1993, pp. 404–413.

[2]Bhutta, B. A., and Lewis, C. H., "Three-Dimensional Hypersonic Nonequilibrium Flows at Large Angles of Attack," AIAA Paper 88-2568, June 1988.

[3]Gupta, R. N., and Lee, K. P., "Thermo-Chemical Nonequilibrium Analysis of Viscous Shock-Layers," AIAA Paper 95-2083, June 1995.

[4]Gnoffo, P. A., Gupta, R. N., and Shinn, J. L., "Conservation Equations and Physical Models for Hypersonic Air Flows in Thermal and Chemical Nonequilibrium," NASA TP-2867, Feb. 1989.

[5]Swaminathan, S., Song, D. J., and Lewis, C. H., "Effects of Slip and Chemical Reaction Models on Three-Dimensional Nonequilibrium Viscous Shock-Layer Flows," *Journal of Spacecraft and Rockets*, Vol. 21, No. 6, 1984, pp. 521–527.

[6]Song, D. J., Swaminathan, S., and Lewis, C. H., "High Altitude Effects on Three-Dimensional Nonequilibrium Viscous Shock-Layer Flows," *Journal of Spacecraft and Rockets*, Vol. 22, No. 6, 1985, pp. 614–619.

[7]Hendricks, W. L., "Slip Conditions with Wall Catalysis and Radiation for Multicomponent Nonequilibrium Air Flow," NASA TM X-64942, June 1974.

[8]Gupta, R. N., Scott, C. D., and Moss, J. N., "Slip-Boundary Equations for Multicomponent Nonequilibrium Air Flow," NASA TP-2452, Nov. 1985.

[9]Swaminathan, S., Kim, M. D., and Lewis, C. H., "Three-Dimensional Nonequilibrium Viscous Shock-Layer Flows over Complex Geometries," AIAA Paper 83-0212, Jan. 1983.

[10]Williams, F. A., *Combustion Theory*, Addison–Wesley, Reading, MA, 1965.

[11]Bird, R. B., Stewart, W. E., and Lightfoot, E. N., *Transport Phenomena*, Wiley, New York, 1960.

[12]Gupta, R. N., Lee, K. P., Zoby, E. V., Moss, J. N., and Thompson, R. A., "Hypersonic Viscous Shock-Layer Solutions over Long Slender Bodies: Part I—High Reynolds Number Flows," AIAA Paper 87-2487, Aug. 1987; also *Journal of Spacecraft and Rockets*, Vol. 27, No. 2, 1990, pp. 175–184.

[13]Gupta, R. N., and Nayani, S. N., "Low-Density Flow Effects for Hypervelocity Vehicle," WRDC-TR-90-3007, Wright–Patterson Air Force Base, OH, March 1990.

[14]Kogan, M. N., *Rarefield Gas Dynamics*, Plenum, New York, 1969.

[15]Adams, M. C., and Probstein, R. F., "On the Validity of Continuum Theory for Satellite and Hypersonic Flight Problems at High Altitudes," *Jet Propulsion*, Feb. 1958, pp. 86–89.

[16]Gupta, R. N., and Simmonds, A. L., "Hypersonic Low-Density Solutions of the Navier-Stokes Equations with Chemical Nonequilibrium and Multicomponent Surface Slip," AIAA Paper 86-1349, June 1986.

[17]Rakich, J. V., "A Method of Characteristics for Steady Three-Dimensional Supersonic Flow with Application to Inclined Bodies of Revolution," NASA TN D-5341, Oct. 1969.

[18]Lee, K. P., Gupta, R. N., Moss, J. N., and Zoby, E. V., "Viscous Shock-Layer Solutions for the Low-Density Hypersonic Flow Past Long Slender Bodies," AIAA Paper 88-0460, Jan. 1988; also *Journal of Spacecraft and Rockets*, Vol. 27, No. 2, 1990, pp. 185–193.

[19]Blottner, F. G., Johnson, M., and Ellis, M., "Chemically Reacting Viscous Flow Program for Multi-Component Gas Mixtures," Sandia Labs. Rept. SC-RR-70-754, Albuquerque, NM, Dec. 1971.

[20]Gupta, R. N., Yos, J. M., Thompson, R. A., and Lee, K. P., "A Review of Reaction Rates and Thermodynamic and Transport Properties for the 11-Species Air Model for Chemical and Thermal Nonequilibrium Calculations to 30000K," NASA TM-101528, Feb. 1989; updated as NASA RP-1232, Aug. 1990.

[21]Armaly, B. F., and Sutton, K., "Viscosity of Multicomponent

Partially Ionized Gas Mixtures Associated with Jovian Entry," *Aerothermodynamics and Planetary Entry*, edited by A. L. Crosbie, Vol. 77, Progress in Astronautics and Aeronautics, AIAA, New York, 1982.

[22]Mason, E. A., and Saxena, S. C., "Approximate Formula for the Thermal Conductivity of Gas Mixtures," *Physics of Fluids*, Vol. 1, No. 5, 1958, p. 361.

[23]Blottner, F. G., "Nonequilibrium Laminar Boundary Layer Flow of Ionized Air," *AIAA Journal*, Vol. 2, No. 11, 1964, pp. 1921–1927.

[24]Murray, A. L., and Lewis, C. H., "Hypersonic Three-Dimensional Viscous Shock-Layer Flows over Blunt Bodies," *AIAA Journal*, Vol. 16, No. 12, 1978, pp. 1279–1286.

[25]Krause, E., "Comment on Solution of a Three-Dimensional Boundary-Layer Flow with Separation," *AIAA Journal*, Vol. 6, March 1969, pp. 575, 576.

[26]Solomon, J. M., Ciment, M., Ferguson, R. E., Bell, J. B., and Wardlaw, A. B., Jr., "A Program for Computing Steady Inviscid Three-Dimensional Supersonic Flow on Reentry Vehicles, Vol. 1, Analysis and Programming; Vol. 11, User's Manual," Rept. Naval Surface Weapons Center/White Oak Lab./Tech. Rept. 77-28, Silver Spring, MD, Feb. 1977.

[27]Lee, K. P., and Gupta, R. N., "Viscous-Shock-Layer Analysis of Hypersonic Flows over Long Slender Vehicles," NASA CR-189614, March 1992.

[28]Kang, S.-W., Jones, W. L., and Dunn, M. G., "Theoretical and Measured Electron-Density Distributions at High Altitudes," *AIAA Journal*, Vol. 11, No. 2, 1973, pp. 141–149.

[29]Jones, W. L., and Cross, A. E., "Electrostatic Probe Measurements of Plasma Parameters for Two Reentry Flight Experiments at 25,000 ft/sec," NASA TN D-6617, April 1972.

[30]Moss, J. N., Cuda, V., and Simmonds, A. L., "Nonequilibrium Effects of Hypersonic Transitional Flows," AIAA Paper 87-0404, Jan. 1987.